PAPER • **OPEN ACCESS**

Spin pumping through nanocrystalline topological insulators

To cite this article: David M Burn *et al* 2023 *Nanotechnology* **34** 275001

OPEN ACCESS
IOP Publishing
Nanotechnology

Nanotechnology **34** (2023) 275001 (8pp)
https://doi.org/10.1088/1361-6528/acc663

Spin pumping through nanocrystalline topological insulators

David M Burn[1], Jheng-Cyuan Lin[2], Ryuji Fujita[2], Barat Achinuq[2], Joshua Bibby[2], Angadjit Singh[2], Andreas Frisk[1], Gerrit van der Laan[1] and Thorsten Hesjedal[2,*]

[1] Diamond Light Source, Harwell Science and Innovation Campus, Didcot, Oxfordshire OX11 0DE, United Kingdom
[2] Clarendon Laboratory, Department of Physics, University of Oxford, Parks Road, Oxford, OX1 3PU, United Kingdom

E-mail: Thorsten.Hesjedal@physics.ox.ac.uk

Received 31 January 2023, revised 10 March 2023
Accepted for publication 21 March 2023
Published 19 April 2023

Abstract

The topological surface states (TSSs) in topological insulators (TIs) offer exciting prospects for dissipationless spin transport. Common spin-based devices, such as spin valves, rely on trilayer structures in which a non-magnetic layer is sandwiched between two ferromagnetic (FM) layers. The major disadvantage of using high-quality single-crystalline TI films in this context is that a single pair of spin-momentum locked channels spans across the entire film, meaning that only a very small spin current can be pumped from one FM to the other, along the side walls of the film. On the other hand, using nanocrystalline TI films, in which the grains are large enough to avoid hybridization of the TSSs, will effectively increase the number of spin channels available for spin pumping. Here, we used an element-selective, x-ray based ferromagnetic resonance technique to demonstrate spin pumping from a FM layer at resonance through the TI layer and into the FM spin sink.

Keywords: spin pumping, topological insulators, nanocrystalline quantum materials, ferromagnetic resonance, x-ray magnetic circular dichroism

(Some figures may appear in colour only in the online journal)

1. Introduction

Modern non-volatile magnetic memory devices are relying on magnetoresistive multilayer structures to read out the magnetic state of domains in a ferromagnetic film. At their core, the multilayers consist of a ferromagnet/non-magnetic/ferromagnet (FM/NM/FM) trilayer structure whose resistance depends on the relative orientation of the magnetization of the two FM layers. Depending on whether or not the NM layer is electrically conducting or insulating, the trilayer is referred to as a spin valve or a magnetic tunnel junction. While it is still common to switch the magnetization of the magnetic bits via an applied external field, all electrical current-driven magnetization reversal has been the key challenge [1], in particular for advanced magnetic random access memory. Among the contenders, spin-transfer and spin–orbit torque (STT [2–4] and SOT [5, 6]) switching have evolved as two possible energy-efficient and scaling-friendly replacements. As SOT is relying on the spin Hall effect [7] in materials with large spin–orbit coupling, heavy metals (HM) such as Pt [5] and Ta [6] are the materials of choice for switching the magnetization state in a HM/FM heterostructure.

The figure-of-merit for SOT heterostructures is the so-called spin Hall angle (SHA), which is essentially the charge-to-spin conversion efficiency, defined as the ratio of the spin and charge current densities. While there is a considerable level of disagreement with regards to the precise value of the

* Author to whom any correspondence should be addressed.

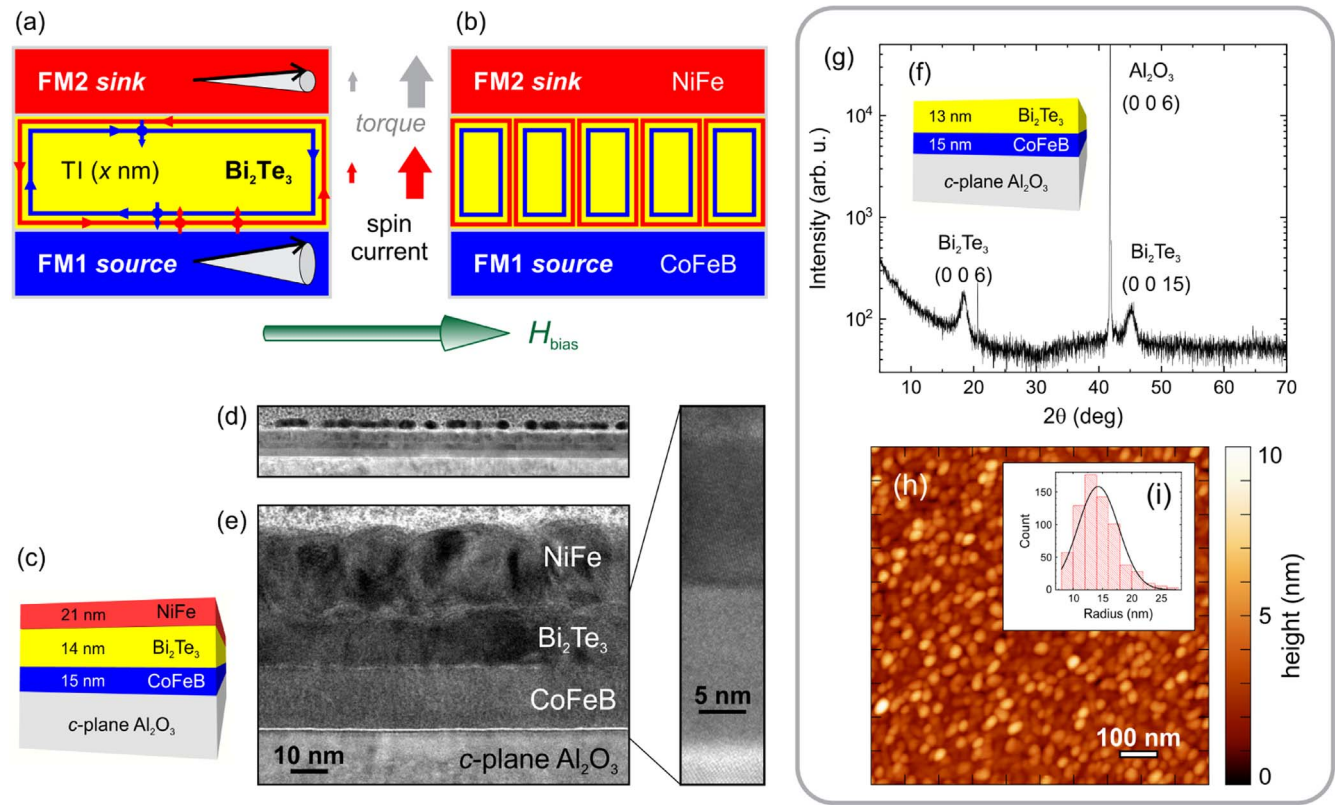

Figure 1. Pseudo spin valve and structural sample properties. Schematic illustrating spin pumping from a ferromagnetic source (FM1) via the TI into the sink layer (FM2) for (a) crystalline and (b) nanocrystalline TI layer, consisting of many grains around which the spin current can flow. (c) NiFe(21)/Bi_2Te_3(14)/CoFeB(15) (thickness in nm) heterostructure on *c*-plane sapphire used for the synchrotron based XFMR measurements. (d) Cross-section low-magnification TEM image of the heterostructure, demonstrating chemically homogeneous films. (e) Higher-magnification TEM image showing that the CoFeB layer is amorphous while the Bi_2Te_3 and FeNi layers are crystalline with grains sizes ranging from 10 to 20 nm. The thicknesses of the layers of 16–17 nm for CoFeB, 13–15 nm for Bi_2Te_3, and 20–24 nm for NiFe agree with the values determined by XRR. On the right-hand side, a close-up of the interfaces between the layers is shown. The properties of the (uncoated) TI layer were further investigated on a Bi_2Te_3(13)/CoFeB(15) bilayer on *c*-plane sapphire (see (f)). (g) Out-of-plane XRD spectrum showing the (0 0 6) and (0 0 15) peaks of Bi_2Te_3, as well as the (0 0 6) peak of the Al_2O_3 substrate. (c) The AFM image shows a homogeneous distribution of small grains, which have an average radius of 15 nm (as shown in the inset in (i)).

SHAs [8], owing to the way the quantity has been measured and the values have been extracted, there is a clear indication that topological insulators (TIs) may have larger room temperature SHAs than common HMs. TIs host conducting, spin-momentum-locked topological surface states (TSSs) [9, 10], which have been reported to lead to large spin-torque effects in adjacent FMs [11–21]. This, in turn, can have a great effect on dynamic properties of magnetic layers in a FM/TI/FM heterostructure, possibly increasing the strength of interaction between the magnetic layers, allowing for quicker response times in magnetization switching [22].

The efficiency of spin-charge effects can be measured in different ways, e.g. by spin transport methods such as spin-torque ferromagnetic resonance (ST-FMR) [11, 15, 18] and spin pumping [13, 14, 17, 23–26], and we refer the reader to the work by Sinova *et al* for a comprehensive review of spin Hall effects [27]. We have previously demonstrated spin pumping *through* an epitaxially grown Bi_2Te_3 layer [28], however, found that the efficiency is limited by the fact that the TSS is extended across the entire film, thereby reducing the spin pumping efficiency through the thickness of the film (see figure 1(a)). On the other hand, in nanocrystalline TIs, for which any dimensions is larger than the thickness below which the 3D TI transitions into a 2D TI [29], a large number of surface states per unit area is taking part in spin pumping (see figure 1(b)). It has been demonstrated that due to quantum confinement in sputtered Bi_xSe_{1-x} films [30, 31], as well as in electron beam deposited Bi_2Se_3 films [32], the spin–orbit torque in $Bi_xSe_{1-x}/Co_{20}Fe_{60}B_{20}$ heterostructures is greatly improved. A similar increase in spin pumping efficiency compared to perfect thin films can be expected for FM/TI/FM trilayer systems. Here, we use XFMR to unambiguously determine the spin pumping efficiency through a nanocrystalline TI layer in a FM/TI/FM trilayer structure, and compare the effect of nanocrystallinity of the TI layer with the result for an epitaxial film.

2. Methods

2.1. Sample preparation and structural characterization

A series of NiFe(20)/Bi_2Te_3(d_{TI})/CoFeB(15)/Al_2O_3 samples was grown (thicknesses in nm) on *c*-plane sapphire substrates

by magnetron sputtering using stoichiometric $Ni_{81}Fe_{19}$ (NiFe), Bi_2Te_3, and $Co_{40}Fe_{40}B_{20}$ (CoFeB) targets (2 inch diameter, 99.9% purity). The CoFeB layer was grown at a substrate temperature of 200 °C (20 W, Ar pressure: 3 mTorr), followed by a 30 min anneal at 400 °C. Next, the Bi_2Te_3 layer was grown at 215 °C, (40 W), and finally the $Ni_{81}Fe_{19}$ at room temperature. The thicknesses of the ferromagnetic CoFeB and NiFe layers were optimized such that a sizeable ferromagnetic resonance could be detected, yet allowing for both the sufficient transmission of x-rays and the observation of spin pump via an increase in the damping constant. The TI growth parameters were optimized to yield small, stoichiometric Bi_2Te_3 grains of reduced dimensions, i.e. aiming at minimizing the volume and maximizing the surface of the TI. The TI thicknesses d_{TI} ranged from 6 to 14 nm. The synchrotron-based measurements were carried out on a sample with a TI thickness of 14 nm, sandwiched between a 15 nm thick CoFeB and a 21 nm thick NiFe layer (schematic shown in figure 1(c)). Transmission electron microscopy (TEM) was carried out on the sample subsequent to the XFMR measurements, showing abrupt interfaces and chemically homogeneous films (low- and higher-magnification images shown in figures 1(d) and (e)).

The structural properties of the samples were analyzed using x-ray reflectivity (XRR) to confirm that layer thicknesses and x-ray diffraction (XRD) to characterize the phase and orientation of the Bi_2Te_3 grains on a Bruker D8 diffractometer using Cu $K\alpha$ radiation. In order to investigate the correlation between Bi_2Te_3 film morphology and XRD pattern, a Bi_2Te_3/CoFeB bilayer was grown with nominally identical growth parameters (figure 1(f)). The XRD spectrum in figure 1(g) shows that the grains are to some degree *c*-axis oriented. Atomic force microscopy (figure 1(h)) was used to determine the size of the TI nanograins for the 14 nm TI layer. From the analysis of the AFM image (grain size distribution shown in figure 1(i), we estimate the average in-plane radius of the grains to be (14.3 ± 3.5) nm. Energy-dispersive x-ray spectroscopy indicates a Bi:Te stoichiometry of 40:60. Cross-sectional TEM samples were prepared by focused ion beam (FIB) milling (JEOL dual beam 4700F), after depositing protective C and Pt layers. The TEM images were collected using a JEOL JEM-2100 microscope operating at 200 kV.

2.2. X-ray absorption and magnetic circular dichroism

Element-specific analysis of both the magnetization as a function of field, and the dynamic magnetization precession as a function of time delay (see section 2.4), was carried out. These synchrotron measurements were performed in the portable octupole magnet system (POMS) end station on beamline I10 at the Diamond Light Source (Oxfordshire, UK). The experiments were performed at room temperature in ultrahigh vacuum in the soft x-ray regime using circularly polarized x-rays tuned to the Fe, Ni, and Co L_3 edges at photon energies of 707, 778, and 852 eV, respectively. The x-ray absorption (XAS) in the magnetic layers was determined from measurements of the substrate luminescence in the visible wavelength range (using x-ray excited optical luminescence, XEOL) [33], using a photodiode placed directly behind the sample, which is proportional to the transmission through the sample [34]. The beam passes through a 100 μm diameter hole in the waveguide which determines the measured area of the sample. The beam is incident at an angle of 35° with respect to the surface normal direction [35]. This choice of incident angle provides sensitivity to both the in-plane and out-of-plane magnetization components. By carrying out XAS measurements with both right- and left-handed circularly polarized x-rays (RCP and LCP), the x-ray magnetic circular dichroism (XMCD) signal is obtained which probes the magnetization component parallel to the beam propagation direction [36, 37]. XAS measurements were performed with both circular light polarizations and magnetic fields H applied parallel and antiparallel to the beam direction. While the XAS sum signal, I_{sum}, is defined as $I^- + I^+$ with $I^- = \frac{1}{2}[I_{LCP}(H) + I_{RCP}(-H)]$ and $I^+ = \frac{1}{2}[I_{RCP}(H) + I_{LCP}(-H)]$, the XMCD signal is $I_{xmcd} = I^- - I^+$ [36]. Element-specific hysteresis loops were measured as a function of magnetic field. Hysteresis loops, obtained at the Co, Fe, and Ni L_3 edges, are shown in figure 2.

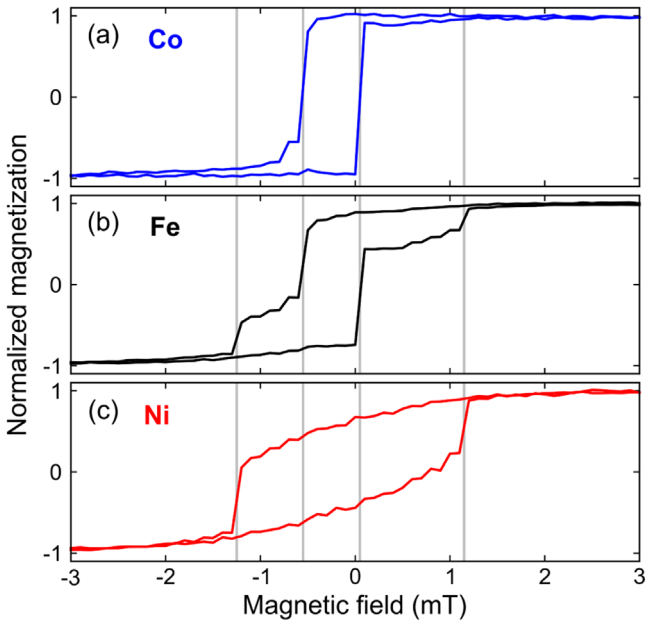

Figure 2. Static element-specific hysteresis loops measured by XMCD at the respective L_3 edges showing the magnetization as a function of applied magnetic field for (a) Co, (b) Fe, and (c) Ni. The single transitions at the Co and Ni edges represent the magnetization switching of the CoFeB and NiFe layers, respectively. The Fe loop, on the other hand, shows the combined behavior of both layers, akin to the magnetic response measured by volume-averaging magnetometry.

2.3. Ferromagnetic resonance (FMR)

Vector network analyzer ferromagnetic resonance (VNA-FMR) measurements [38, 39] were also performed *in situ* to characterize the dynamic magnetization behavior of the entire sample stack, and to identify the resonance modes suitable for XFMR analysis. Here, the radio freqency (RF) power

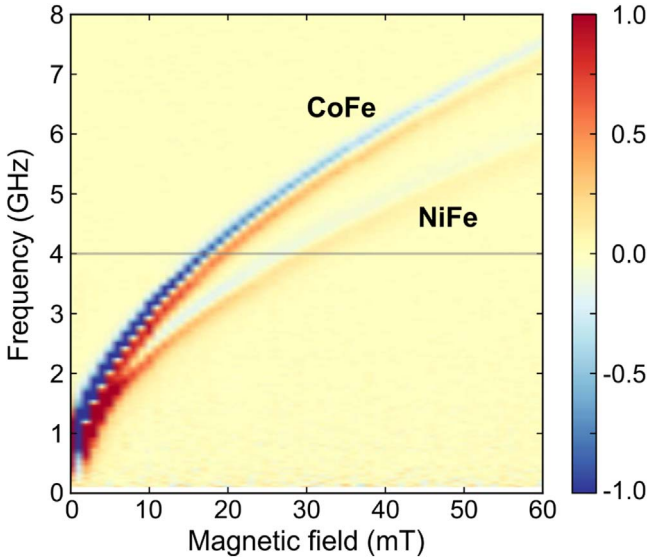

Figure 3. Magnetic resonance modes revealed by VNA-FMR measurements as a function of RF frequency and magnetic bias field. Both the RF and bias field are applied in-plane and perpendicular to each other. The colors indicate the derivative of the RF power transmission, S_{21}, with respect to the magnetic field, which represents the changes in RF power absorbed by the sample. The horizontal line at 4 GHz indicates the mode crossings probed by XFMR measurements.

transmission, S_{21}, through the coplanar waveguide (CPW) is measured, indicating changes in the power absorption by the magnetic sample. This absorption is measured as a function of both RF frequency and bias magnetic field, thereby mapping out the behavior of the magnetic resonance modes. The result for the 14 nm thick Bi_2Te_3 sample is shown in figure 3.

2.4. XFMR

Capable of applying magnetic fields of up to 0.6 T in any direction, POMS is a preferred and versatile end station well-suited not only for VNA-FMR measurements, but also for synchrotron radiation based studies [36]. To achieve layer-resolved FMR of chemically distinct layers, x-ray detected FMR (XFMR) is the method of choice [28, 34, 40–60] In XFMR, XMCD [37] (and more rarely x-ray magnetic linear dichroism [61]) is employed to measure the element-specific dynamic signal while exciting precessional dynamics in the magnetic layers. An RF magnetic field generated from a CPW is coupled to the sample, which is mounted in a flip-chip configuration, i.e. with the top layer of the heterostructure facing the CPW (see figure 5(a)). In this transmission geometry, the XEOL signal from the transparent substrate is detected by a photodiode placed directly behind the sample. Recently, the XFMR family of techniques was considerably extended by selectively probing specific dynamic modes in diffractive FMR [62, 63] and reflectometry FMR [64, 65], which make use of an x-ray reflection geometry. The RF field is applied in the plane of the sample along the x-ray beam direction. An additional bias magnetic field is also applied in-plane and perpendicular to both the RF field and x-ray beam direction, as illustrated in figure 5(a). The RF signal is phase locked to integer multiples of the synchrotron master clock, ~500 MHz, which provides the frequency of the pulsed x-ray source. This synchronization allows us to perform stroboscopic measurements of the magnetization dynamics. The dynamic signal was measured as a function of a variable time delay between the RF excitation and pulsed x-ray probe. This allows for the time-dependent dynamic evolution of the magnetization precession to be mapped out. A lock-in detection approach was employed to enhance the dynamic signal where the phase of the RF excitation was modulated by 180° at 3 kHz. For recent reviews and further details on XFMR as well as the experimental setup used in our experiment, we refer to [55, 66]. XFMR delay scans at the Co and Ni L_3 edges are shown in figures 4(b) and (c).

3. Results and discussion

First, the static layer-resolved magnetization behavior of the 14 nm Bi_2Te_3 trilayer sample was investigated using XMCD. Figure 2 shows the element-specific magnetization for Co, Fe, and Ni as a function of magnetic field applied along the beam direction. For each element, a hysteresis loop is observed with relatively sharp transitions between discrete magnetization states. The magnetization is easily saturated in these films within a few mT.

The hysteresis loops measured at the Ni and Co edges independently probe the magnetization in the NiFe and CoFeB layers, respectively. These loops are dominated by a single transition in the magnetic field, representing the field required to reverse the magnetization in that layer.

Since measurement at the Fe edge probes both the NiFe and CoFe layers, the hysteresis loop reveals a combined magnetic response of both layers, exhibiting both characteristic steps. The two unique switching fields demonstrate that the magnetization in the two layers is not directly coupled through the exchange interaction. The TI layer forms a continuous layer separating the two ferromagnetic layers.

The NiFe layer reverses at the higher field of 1.2 mT, whilst the magnetization in the CoFeB reverses at a lower field. Furthermore, there is a large asymmetry in the CoFeB reversal fields. In this context, the Fe XMCD hysteresis loop serves an important role, namely that in the Fe hysteresis the NiFe loop is symmetric while the FeCoB loop is not. This convincingly excludes that the asymmetry of the CoFeB loops would be due to remanence of the electromagnet, but rather due to exchange bias. A discussion of possible reasons for this observation will be given in the context of the FMR experiment.

VNA-FMR measurements were used to provide an initial characterization of the magnetization dynamics within the sample. Figure 3 shows the changes in the RF absorption with respect to the applied field, mapped as a function of both frequency and applied field. Here, two lines with sharp changes in the absorption indicate ferromagnetic resonance modes which follow a Kittel curve-like behavior. The two modes can be attributed to the dynamic ferromagnetic resonance modes in the two ferromagnetic layers. The higher

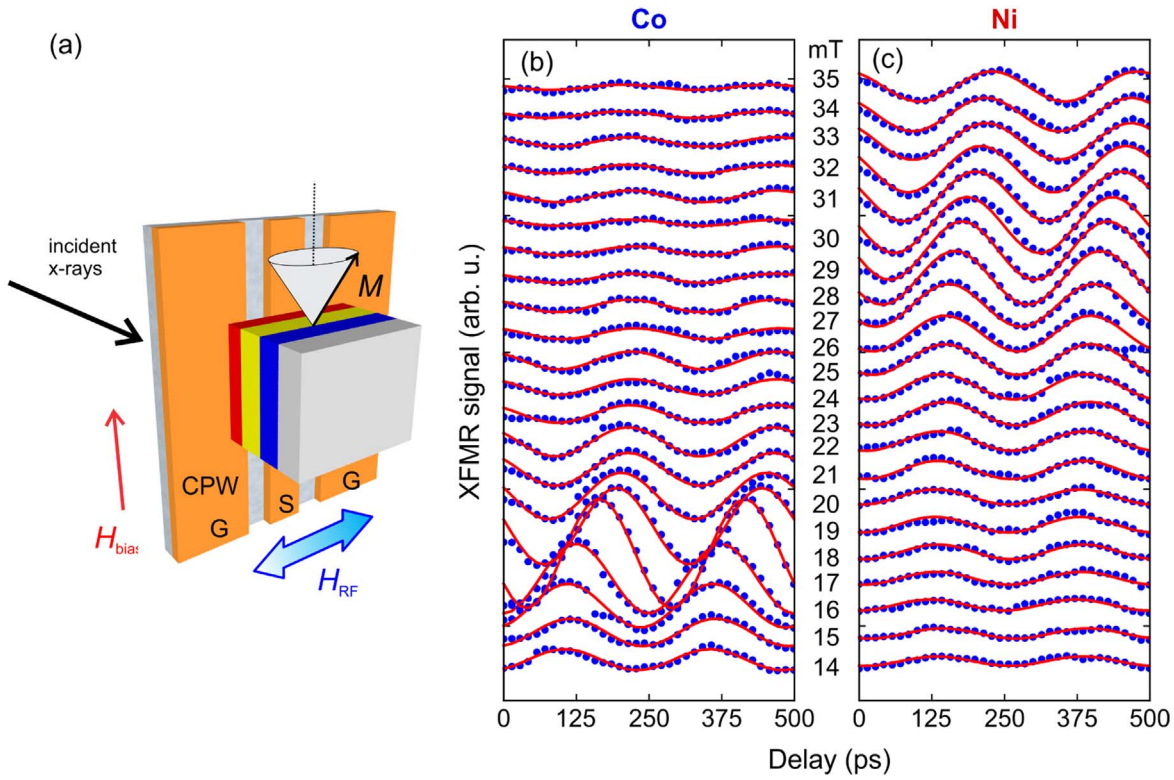

Figure 4. XFMR sample setup and delay scans. (a) Schematic of the sample mounted face-down onto the CPW. (b), (c) XFMR signals as a function of time delay for both the (a) Co and (b) Ni L_3 edges for various applied magnetic fields. The plots have been offset for clarity. Sinusoidal functions (red lines) have been fitted to the data.

frequency mode is that of the CoFeB layer, while the weaker mode at lower frequencies originates from the NiFe layer. The identification of the modes has been achieved by the XFMR measurements, as will be discussed below. Note that for weakly coupled ferromagnetic layers, i.e. in systems with well-separated resonance modes, spin pumping from one layer to the other is not detectable in VNA-FMR.

Returning to the possible origins of exchange bias of the CoFeB layer, we note that the Kittel curve for CoFeB does not go through the origin, i.e. that there is a finite frequency value at zero field. By performing density functional theory calculations, Kim *et al* found that the large spin–orbit coupling of Bi (in the Bi_2Te_3 TI layer) enhances the exchange coupling to the ferromagnetic layer [67]. Further, in experiments on Bi_2Se_3 layers on yttrium iron garnet (YIG), a large interfacial in-plane magnetic anisotropy and an increasing exchange effective field were found, evidenced by an offset in the Kittel curve akin to the one observed in our case as well [68]. By carrying out a thickness-dependent study of the interfacial anisotropy, the maximum effect was found in the case when the TI film approaches its 2D limit, i.e. 7 nm for Bi_2Te_3 on YIG [68]. Given that the nanocrystalline Bi_2Te_3 film investigated here was 14 nm, i.e. twice as thick, it is not clear whether the exchange bias effect is due to a lateral or vertical confinement effect, and further studies are planned.

XFMR probes the element-, and thus layer-specific magnetization dynamics in the magnetic heterostructure. A frequency of 4 GHz was chosen (a multiple of the synchrotron's master clock frequency of 500 MHz), as relatively low frequencies normally yield stronger XFMR signals and as the CoFeB and NiFe resonances are clearly separated in field at this frequency (see figure 3). Figure 4 shows the dynamic XFMR signal as a function of time delay between the RF excitation and x-ray probe. This is shown for a variety of different magnetic bias fields across the resonances, where the bias is applied perpendicular to both the RF field and beam propagation direction.

Figure 4 shows XFMR delay scans for the photon energy tuned to the Co and Ni edges, which vary sinusoidally with time, matching the RF excitation frequency of 4 GHz. The amplitude of this signal depends on the bias field, peaking when the resonance conditions for the respective layer are met. At the Co edge, probing the CoFeB layer, the resonance occurs at 18 mT while at the Ni edge (probing the NiFe layer) the resonance is at 30 mT. Both resonance fields are consistent with the VNA-FMR results shown in figure 3. Following the maxima across the resonance, it is also clear that the signals show a phase change (figure 4).

Sinusoidal fits to the XFMR data as a function of delay time, indicated by the solid red lines in figure 4, yield the amplitude and phase of the dynamic signal for each applied field. These extracted parameters are collected in figure 5 as a function of applied bias field for both Co and Ni. The two resonances at 18 mT for Co and 30 mT for Ni are clearly visible as peaks in the amplitude plots, accompanied by a 180° phase shift. The lines in figure 5(a) show a Lorentzian fit to the amplitude data and in (b) show an arctan function

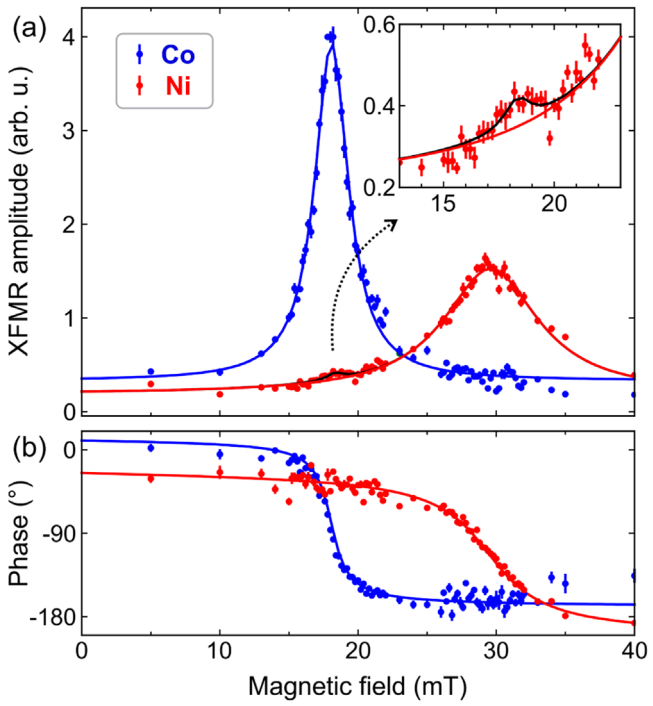

Figure 5. XFMR (a) amplitude and (b) phase of the dynamic signal as a function of magnetic bias field. Measurements at the Co and Ni edges show peaks in amplitude with a corresponding 180° phase shift at the resonances at 18 and 30 mT, respectively. The lines show Lorentzian fits to the amplitude data and an arctan overlaid as guide to the eye for the phase data. The inset to panel (a) shows a magnified section of the Ni amplitude data around 18 mT.

which provides a guide-to-the-eye of the 180° phase shift with the same center field as for the Lorentzians.

In addition to the NiFe resonance at 30 mT, the Ni amplitude data in figure 5(a) also shows a small deviation from the Lorentzian lineshape at 18 mT, i.e. at the CoFeB resonance field, which is more clearly visible in the inset to panel (a). Note that for the measurement at the Ni edge, XFMR is not sensitive to the CoFeB layer dynamics. This additional dynamic contribution has been further analyzed. The black line in figure 5(a) (and in the inset) shows the best fit of a model containing the sum of two Lorentzians, one describing the NiFe resonance at 30 mT and an additional weaker component at 18 mT. This extended model provides a better fit to the data in this low field region. The CoFeB resonance is at (18.08 ± 0.02) mT. The additional peak in the Ni data is at (18.3 ± 0.3) mT, i.e. both are occurring at the same field within the errors.

The additional peak in the Ni dynamic signal that occurs at the same field and frequency as the resonance in the CoFeB layer indicates dynamic coupling between the two layers. Note that the two ferromagnetic layers are not directly exchange-coupled, as can be seen from figure 2. This suggests that a dynamic spin current from the CoFeB layer is being pumped through the TI and absorbed by the NiFe layer, which is now precessing at the same frequency as the CoFeB layer. The observed XFMR response of the NiFe layer at the resonance condition of the CoFeB layer confirms the dynamic character of the coupling between both layers [55, 69]. For dynamic exchange coupling, i.e. spin pumping, the magnetic field is imaginary, resulting in a 90° phase change. In this case, the field-dependent precession of NiFe layer shows a symmetric (unipolar) peak in the amplitude and a dispersive (bipolar) peak in the phase. In contrast, for static exchange coupling, the effective field in the NiFe layer is aligned along the magnetization of the CoFeB layer. In this case, the field-dependent precession of the NiFe would show a bipolar peak in the amplitude and a symmetric unipolar peak in the phase. While the phase curve at 18 mT does not allow an unambiguous interpretation due to the statistics, the amplitude curve convincingly shows a unipolar peak, which is characteristic for spin pumping.

Note that the data presented here are the first observation of spin pumping *through* a TI layer in the XFMR amplitude. In our earlier work on epitaxial TI layers, we were only able to observe very weak spin pumping via the more sensitive phase signal [28]. While a decay length of 8 nm was observed for an epitaxial Bi_2Se_3 layer (in a $Co_{50}Fe_{50}$/TI/NiFe heterostructure, i.e. a vanishing spin pumping effect between the ferromagnetic layers [28], the use of a nanocrystalline TI interlayer clearly supports spin pumping through a 14 nm thick TI film. Owing to the strongly damped spin transfer in the epitaxial system, a quantitative estimation of the improvement using nanocrystalline films is not possible. In the future, we intend to carry out more systematic measurements of the influence of TI film thickness, grain size and distribution, and temperature on the spin transfer phenomena in these promising materials systems. In particular, we hope to be able to resolve the anticipated crossover from 3D to 2D TI behavior, and the oscillatory switching from topologically trivial to non-trivial behavior in the 2D regime, as a function of TI layer thickness [70].

4. Conclusion

In summary, trilayer structures of CoFeB/TI/NiFe have been grown where the growth of the TI layer has been optimized to be in a granular texture. Soft x-ray measurements were used to provide element-specific measurements on the two magnetic layers which are shown to act independently without any static exchange coupling between the two layers. The XFMR element-specific probe of the magnetization dynamics was used to probe independent magnetic resonances from both of the ferromagnetic layers. Additional dynamic precessional behavior was measured in the NiFe layer which occurred at the field and frequency for the resonance in the CoFeB layer. In the absence of exchange coupling between the layers, this was attributed to AC spin pumping from the CoFeB into the NiFe which is used to drive the precession. Since a consistent layer of TI exists between the ferromagnetic layers this indicates the spin pumping occurs over the surface states of the grains within the TI layer. Engineering of the TI layer to have a greater proportion of surface states is a useful technique to control the level of spin pumping in future devices.

Acknowledgments

We acknowledge Diamond Light Source for provision of beamtime using the portable octupole magnet system on beamline I10 under proposals MM21872 and MM27487, and RCaH for their hospitality. Financial support from the John Fell Fund (University of Oxford), the Oxford-ShanghaiTech collaboration project, the Leverhulme Trust (RPG-2020-358), and the UK Skyrmion Project (Engineering and Physical Sciences Research Council, EP/N032128/1) is acknowledged.

Data availability statement

All data that support the findings of this study are included within the article (and any supplementary files).

Conflict of interest

The authors declare no competing financial interest.

ORCID iDs

David M Burn https://orcid.org/0000-0001-7540-1616
Jheng-Cyuan Lin https://orcid.org/0000-0002-5085-3234
Ryuji Fujita https://orcid.org/0000-0001-8557-5812
Barat Achinuq https://orcid.org/0000-0001-6446-8209
Joshua Bibby https://orcid.org/0000-0002-2975-7969
Angadjit Singh https://orcid.org/0000-0003-4922-4956
Andreas Frisk https://orcid.org/0000-0001-9234-0907
Gerrit van der Laan https://orcid.org/0000-0001-6852-2495
Thorsten Hesjedal https://orcid.org/0000-0001-7947-3692

References

[1] Katine J A, Albert F J, Buhrman R A, Myers E B and Ralph D C 2000 *Phys. Rev. Lett.* **84** 3149–52
[2] Slonczewski J C 1996 *J. Magn. Magn. Mater.* **159** L1–7
[3] Berger L 1996 *Phys. Rev.* B **54** 9353–8
[4] Ralph D C and Stiles M D 2008 *J. Magn. Magn. Mater.* **320** 1190–216
[5] Miron I M, Garello K, Gaudin G, Zermatten P J, Costache M V, Auffret S, Bandiera S, Rodmacq B, Schuhl A and Gambardella P 2011 *Nature* **476** 189–93
[6] Liu L, Pai C F, Li Y, Tseng H W, Ralph D C and Buhrman R A 2012 *Science* **336** 555–8
[7] Hirsch J E 1999 *Phys. Rev. Lett.* **83** 1834–7
[8] Liu L, Buhrman R and Ralph D 2011 arXiv:1111.3702
[9] Chen Y L *et al* 2009 *Science* **325** 178–81
[10] Moore J E 2010 *Nature* **464** 194–8
[11] Mellnik A R *et al* 2014 *Nature* **511** 449–51
[12] Fan Y *et al* 2014 *Nat. Mater.* **13** 699–704
[13] Shiomi Y, Nomura K, Kajiwara Y, Eto K, Novak M, Segawa K, Ando Y and Saitoh E 2014 *Phys. Rev. Lett.* **113** 196601
[14] Deorani P, Son J, Banerjee K, Koirala N, Brahlek M, Oh S and Yang H 2014 *Phys. Rev.* B **90** 094403
[15] Wang Y, Deorani P, Banerjee K, Koirala N, Brahlek M, Oh S and Yang H 2015 *Phys. Rev. Lett.* **114** 257202
[16] Rojas-Sánchez J C *et al* 2016 *Phys. Rev. Lett.* **116** 096602
[17] Wang H, Kally J, Lee J S, Liu T, Chang H, Hickey D R, Mkhoyan K A, Wu M, Richardella A and Samarth N 2016 *Phys. Rev. Lett.* **117** 076601
[18] Kondou K, Yoshimi R, Tsukazaki A, Fukuma Y, Matsuno J, Takahashi K S, Kawasaki M, Tokura Y and Otani Y 2016 *Nat. Phys.* **12** 1027–31
[19] Han J, Richardella A, Siddiqui S A, Finley J, Samarth N and Liu L 2017 *Phys. Rev. Lett.* **119** 077702
[20] Wang Y *et al* 2017 *Nat. Commun.* **8** 1364
[21] Yokoyama T, Zang J and Nagaosa N 2010 *Phys. Rev.* B **81** 241410
[22] Hoffmann A and Bader S D 2015 *Phys. Rev. Appl.* **4** 047001
[23] Tserkovnyak Y, Brataas A and Bauer G E 2002 *Phys. Rev.* B **66** 224403
[24] Mosendz O, Pearson J E, Fradin F Y, Bauer G E W, Bader S D and Hoffmann A 2010 *Phys. Rev. Lett.* **104** 046601
[25] Shaw J M, Nembach H T and Silva T J 2012 *Phys. Rev.* B **85** 054412
[26] Jamali M, Lee J S, Jeong J S, Mahfouzi F, Lv Y, Zhao Z, Nikolic B K, Mkhoyan K A, Samarth N and Wang J P 2015 *Nano Lett.* **15** 7126–32
[27] Sinova J, Valenzuela S O, Wunderlich J, Back C H and Jungwirth T 2015 *Rev. Mod. Phys.* **87** 1213–60
[28] Baker A A, Figueroa A I, Collins-McIntyre L J, van der Laan G and Hesjedal T 2015 *Sci. Rep.* **5** 7907
[29] Zhang Y *et al* 2010 *Nature Phys.* **6** 584–8
[30] Mahendra D C *et al* 2018 *Nat. Mater.* **17** 800–7
[31] Mahendra D C, Chen J Y, Peterson T, Sahu P, Ma B, Mousavi N, Harjani R and Wang J P 2019 *Nano Lett.* **19** 4836–44
[32] Singh B B, Jena S K, Samanta M, Biswas K and Bedanta S 2020 *ACS Appl. Mater. Interfaces* **12** 53409–15
[33] Vaz C A F, Moutafis C, Buzzi M and Raabe J 2013 *J. Electron Spectrosc. Relat. Phenom.* **189** 1–4
[34] Gladczuk L, Gladczuk L, Dluzewski P, van der Laan G and Hesjedal T 2021 *Phys. Stat. Sol. (RRL)* **15** 2100137
[35] Stöhr J 1999 *J. Magn. Magn. Mater.* **200** 470–97
[36] van der Laan G and Figueroa A I 2014 *Coord. Chem. Rev.* **277–278** 95–129
[37] van der Laan G 2013 *J. Phys.: Conf. Ser.* **430** 012127
[38] Kittel C 1948 *Phys. Rev.* **73** 155–61
[39] Farle M 1998 *Rep. Prog. Phys.* **61** 755
[40] Goulon J, Rogalev A, Wilhelm F, Jaouen N, Goulon-Ginet C, Goujon G, Ben Youssef J and Indendom M V 2005 *JETP Lett.* **82** 696–701
[41] Goulon J, Rogalev A, Wilhelm F, Jaouen N, Goulon-Ginet C and Brouder C 2006 *Eur. Phys. J.* B **53** 169–84
[42] Arena D A, Vescovo E, Kao C C, Guan Y and Bailey W E 2006 *Phys. Rev.* B **74** 064409
[43] Guan Y, Bailey W E, Kao C C, Vescovo E and Arena D A 2006 *J. Appl. Phys.* **99** 08J305
[44] Guan Y, Bailey W E, Vescovo E, Kao C C and Arena D A 2007 *J. Magn. Magn. Mater.* **312** 437–378
[45] Boero G, Mouaziz S, Rusponi S, Bencok P, Nolting F, Stepanow S and Gambardella P 2008 *New J. Phys.* **10** 013011
[46] Arena D A, Ding Y, Vescovo E, Zohar S, Guan Y and Bailey W E 2009 *Rev. Sci. Instrum.* **80** 083903
[47] Boero G, Rusponi S, Kavich J, Lodi Rizzini A, Piamonteze C, Nolting F, Tieg C, Thiele J U and Gambardella P 2009 *Rev. Sci. Instrum.* **80** 123902
[48] Marcham M K *et al* 2011 *J. Appl. Phys.* **109** 07D353
[49] Marcham M K *et al* 2013 *Phys. Rev.* B **87** 180403(R)

[50] Stenning G B G *et al* 2015 *New J. Phys.* **17** 013019
[51] Figueroa A I, Baker A A, Collins-McIntyre L J, Hesjedal T and van der Laan G 2016 *J. Magn. Magn. Mater.* **400** 178–83
[52] Baker A A, Figueroa A I, Love C J, Cavill S A, Hesjedal T and van der Laan G 2016 *Phys. Rev. Lett.* **116** 047201
[53] Li J *et al* 2016 *Phys. Rev. Lett.* **117** 076602
[54] Durrant C J *et al* 2017 *Phys. Rev.* B **96** 144421
[55] van der Laan G 2017 *J. Electron Spectrosc. Relat. Phenom.* **220** 137–46
[56] Emori S *et al* 2020 *Nano Lett.* **20** 7828–34
[57] Pogoryelov Y *et al* 2020 *Phys. Rev.* B **101** 054401
[58] Klewe C *et al* 2020 *Synchrotron Radiat. News* **33** 12–9
[59] Dabrowski M *et al* 2020 *ACS Appl. Mater. Interfaces* **12** 52116–24
[60] Gladczuk L, Gladczuk L, Dluzewski P, Lasek K, Aleshkevych P, Burn D M, van der Laan G and Hesjedal T 2021 *Phys. Rev.* B **103** 064416
[61] Klewe C *et al* 2022 *New J. Phys.* **24** 013030
[62] Burn D M, Zhang S, Zhai K, Chai Y, Sun Y, van der Laan G and Hesjedal T 2020 *Nano Lett.* **20** 345–52
[63] Burn D M, Zhang S L, van der Laan G and Hesjedal T 2022 *Phys. Rev.* B **106** 174409
[64] Burn D M, Zhang S L, Yu G Q, Guang Y, Chen H J, Qiu X P, van der Laan G and Hesjedal T 2020 *Phys. Rev. Lett.* **125** 137201
[65] Burn D M, Zhang S L, van der Laan G and Hesjedal T 2021 *AIP Adv.* **11** 015327
[66] van der Laan G and Hesjedal T 2023 arXiv:2301.03256
[67] Kim J, Kim K W, Wang H, Sinova J and Wu R 2017 *Phys. Rev. Lett.* **119** 027201
[68] Fanchiang Y T, Chen K H M, Tseng C C, Chen C C, Cheng C K, Yang S R, Wu C N, Lee S F, Hong M and Kwo J 2018 *Nat. Commun.* **9** 223
[69] Baker A A, Figueroa A I, Pingstone D, Lazarov V K, van der Laan G and Hesjedal T 2016 *Sci. Rep.* **6** 35582
[70] Liu C X, Zhang H, Yan B, Qi X L, Frauenheim T, Dai X, Fang Z and Zhang S C 2010 *Phys. Rev.* B **81** 041307